The role of cathode architecture and anion interactions on the performance of Al-substituted α -Ni(OH)₂ in rechargeable Ni–Zn cells

Samuel W. Kimmel,^{1,2} Ryan H. DeBlock,² Jaret A. Manley,³ Cory M. Silguero,³ Debra R. Rolison,^{2*} and Christopher P. Rhodes^{1,3*}

E-mail addresses: debra.r.rolison.civ@us.navy.mil (D. Rolison); cprhodes@txstate.edu (C. Rhodes)

ARTICLE INFO

Keywords
Nickel hydroxide nanosheets
Microwave synthesis
Electrode architecture
Alkaline batteries
Nickel–zinc batteries

ABSTRACT

Rechargeable alkaline Ni-Zn batteries configured with Zn-sponge anodes provide an energy dense, safe alternative to Li-ion batteries for a wide range of risk-averse applications. Advanced cathodes that provide high rate and capacity performance are needed to match that of Zn sponge anodes. We show that aluminum-substituted nickel hydroxide, α-Ni_{0.9}Al_{0.1}(OH)₂, expressed in a nanosheet morphology, can be directly deposited onto a flexible carbon nanofiber paper (CNP) using a rapid and scalable two-step microwave-assisted hydrothermal reaction. The architected electrode (α-Ni_{0.9}Al_{0.1}(OH)₂@CNP) wires the energy-storing Ni to the carbon scaffold, resulting in high capacity and stable cycling in Ni-Zn cells, performance not obtained using conventional powder-composite cathodes. The growth reaction time and temperature influence mass loading, thickness, crystal structure, the ratio of interlayer "free"-to-lattice metal-coordinated "bound" nitrates, and electrochemical performance. The architected α-Ni_{0.9}Al_{0.1}(OH)₂@CNP||Zn sponge alkaline cell provides unprecedented performance, delivering high discharge capacity, storage of >1.4 electrons per Ni, good rate capability, excellent capacity retention, and high mass loading. Architected electrodes that combine 3D electronic wiring and structured active material provide a pathway to energy dense, safe, rechargeable Ni-Zn batteries and offer approaches to improve the electrochemical performance of a broad class of layered materials for multiple battery chemistries.

1. Introduction

Affordable and safe batteries are needed to decarbonize the electric grid and store the energy that runs electric vehicles (EVs), auxiliary power systems, and portable devices. Lithium-ion batteries have been widely adopted for all of these uses [1], despite being plagued with sustainability issues [2], high cost [1,3], supply-chain insecurities [2], and extraction consequences that risk depleting scarce water supplies or violating basic human rights [4]. But Li-ion's most significant problem is its safety record, with numerous examples of battery-related fires and explosions [5].

Alternatives to Li-ion batteries include aqueous zinc-based batteries (such as nickel–zinc, manganese–zinc, and silver–zinc) that use alkaline electrolytes and offer increased safety and lower toxicity relative to

¹ Materials Science, Engineering, and Commercialization Program, Texas State University, 601 University Drive, San Marcos, TX 78666, USA

² U.S. Naval Research Laboratory, Surface Chemistry Branch (Code 6170), 4555 Overlook Avenue SW, Washington, D.C. 20375, USA

³ Department of Chemistry and Biochemistry, Texas State University, 601 University Drive, San Marcos, TX 78666, USA

^{*}Corresponding authors.

Li-ion batteries [3,6]. Zinc, a historically non-rechargeable battery anode, has been widely accepted by consumers for decades [3]. Rechargeable nickel–zinc (Ni–Zn) has high specific energy (60–110 Wh kg⁻¹) and energy density (90–250 Wh L⁻¹), reasonable power capability, excellent abuse tolerance (nonflammable, safe aqueous electrolyte), and does not require a battery management system, all of which make Ni–Zn batteries a compelling alternative to Li-ion batteries [7].

Formulating zinc in a sponge form factor converts a once poorly rechargeable anode into a safe, materially abundant, cost-compelling competitor to Li-based anodes [8-15]. In alkaline electrolytes, an architected zinc anode enables high Zn utilization (depth-of-discharge, DOD_{Zn}), achieving >95% DOD_{Zn} on a single discharge or >150 cycles at 40% DOD_{Zn}, while maintaining dendrite-free cycling [8-15]. Projections of a Ni–Zn sponge battery pack show that the specific energy is comparable or superior to a Li-ion pack that includes catastrophe management systems [12]. The performance of present alkaline nickel cathodes is adequate for use with conventional zinc anodes, but a single Zn sponge outperforms multiple replacements of commercially harvested Ni-cathodes in a rechargeable configuration [8]. Commercial Ni–Zn batteries use alkaline-stable β -Ni(OH)₂ cathodes that capture \sim 90% of its one-electron Ni^{2+/3+} redox capacity (theoretical: 289 mAh g⁻¹) [16], while the Zn-sponge anode can reversibly store two electrons per Zn: Eqs. (1–3).

$$2 \text{ Ni(OH)}_2 + [\text{Zn(OH)}_4]^{2-} \leftrightarrow 2 \text{ NiOOH} + \text{Zn} + 2\text{H}_2\text{O} + 2 \text{ OH}^-$$
 (1)

$$Ni(OH)_2 + OH^- \leftrightarrow NiOOH + H_2O + e^-$$
 (2)

$$Zn + 4 OH^{-} \leftrightarrow [Zn(OH)_{4}]^{2-} + 2 e^{-}$$
 (3)

The capacity of β -phase Ni(OH)₂ cathodes constrains the energy and power performance of Ni–Zn cells that incorporate Zn-sponge anodes. A hydrated phase of Ni(OH)₂, α -Ni(OH)₂, has a higher theoretical capacity (482 mAh g⁻¹) because the average 3.67+ oxidation state of Ni in the γ -NiOOH charged product enables greater than one-electron transfer per Ni site. That higher degree of charge storage is facilitated by incorporating ions into the oxyhydroxide structure [17]. A Ni cathode using higher capacity α -Ni(OH)₂ would increase the system-level energy density of a Ni–Zn battery at a given Zn depth-of-discharge, but α -Ni(OH)₂ suffers from phase-stability in alkaline electrolytes [7,17,18]. Our prior work shows that using microwave-synthesized Al-substituted α -Ni(OH)₂ nanosheets in powder-composite cathodes and cycling them vs. Zn-sponge anodes increases phase stability and discharge capacity relative to unsubstituted α -Ni(OH)₂ nanosheets [18]. Although capacity retention improves with Al-substituted α -Ni(OH)₂, the cell still exhibits fade with cycling [18]. We attribute the delayed but still present capacity fade to less-than-full utilization of α -Al_{0.13}Ni_{0.87}(OH)₂ within the micron-sized agglomerates characteristic of a traditional powder-composite electrode structure.

While the average Ni oxidation state in γ -NiOOH is 3.67, galvanostatic experiments with planar films indicate that α -Ni-cathodes do not fully reduce from Ni^{3.67+} to Ni²⁺ when the Ni(OH)₂ layer is > 10 nm thick [17]. As α -Ni(OH)₂ film thickness increases, usable capacity decreases because of electrochemical isolation within the film [17,19]. Ellipsometric data obtained for planar Ni(OH)₂ thin films in alkaline electrolytes fit a model in which differences in electronic conductivity between Ni(OH)₂ and NiOOH create electronically isolated regions of untapped active material [19]. Forcing further oxidation of the thin film electrolyzes water at the NiOOH surface, a parasitic reaction in a Ni–Zn battery.

Synthesizing nanostructured Ni(OH)₂ in the presence of carbon using hydrothermal/precipitation routes produces carbon-associated active materials that nonetheless must still be formulated into a powder-composite cathode [20-32]. These composited cathodes exhibit higher discharge capacity, better capacity retention, and/or improved rate performance for a wide range of electrochemical devices, yet cannot reach battery-relevant high mass loading and cycle stability, thus limiting system-level energy density [33,34].

As an alternative to 2D planar electrodes and powder composites, high surface-area threedimensional (3D) hierarchically wired conductive networks can be modified with charge-storing material [34-37]. Depositing nanostructured electrode materials at 3D-wired substrates shortens diffusion pathways through the electrode material to the electronic scaffold [34-37]. Predominant 3D-wired conductive frameworks are metal foams/meshes or carbon networks. Microwave synthesis has grown nanosheets of Ni/Co/Mn(OH)₂ [38], Ni/Co(OH)₂ [39], Co-Mo Mo(OH)₂ [40], and nanoflakes of Ni/Fe/Co(OH)₂ [41] onto a nickel-foam current collector, while Co/Al-layered hydroxides have been grown hydrothermally on reduced graphene oxide-decorated nickel foam [42]. Carbonaceous networks are more appealing than metallic networks because the lower mass relative to metallic foams increases the system-level energy density of the device [34,43]. In a three-electrode configuration, a NiAlCo(OH)₂@carbon nanotube electrode has high capacity (320 mAh g⁻¹) but only 184 mAh g⁻¹ when tested in a Ni–Zn cell at a battery-irrelevant low mass loading (1 mg cm⁻²) [27]. Nanocomposite cathodes with high mass loadings (> 10 mg cm⁻²) are reported for β -Ni(OH)₂@carbon nanofiber powder composites [25] and binder-free NiCo(OH)₂@CuO/Cu-foam but these cathodes exhibit low in-cell discharge capacity (184 and 245 mAh g^{-1} , respectively). 3D-wired Ni cathodes with high mass loadings that deliver high capacity with capacity retention in Ni-Zn cells at battery-relevant and fast discharge rates have not been reported.

In addition to improving electron wiring through the volume of the electrode structure, designing high performance Ni-cathodes requires further understanding of the local structure of anions and other species within the interlayer region of Ni(OH)₂ and their effect on battery performance. When synthesizing layered materials such as α -Ni(OH)₂, water, solvent, and other ions are incorporated between the layers or in hydroxyl lattice positions [44]. The interlayer anions within α -Ni(OH)₂ influence proton diffusion coefficient, electrochemical impedance, discharge capacity, and cycle stability in batteries [45,46] and capacitors [47,48]. But how anions coordinate within layered α -Ni(OH)₂ battery materials, how these anion interactions can be synthetically controlled, and how anion interactions affect the electrochemical performance of Ni(OH)₂ battery cathodes have not been significantly studied.

We report an architected Ni cathode, α -Ni_{0.9}Al_{0.1}(OH)₂ deposited on a 3D electronically wired carbon nanofiber paper (CNP), that provides high electrochemical performance and incorporates coordinated anions within the layered hydroxide. Our work shows how controlled synthetic conditions can be used to nucleate and grow a uniform α -Ni_{0.9}Al_{0.1}(OH)₂ coating onto carbon nanofibers comprising a binder-less architected paper electrode. We find that distinct anion coordination environments, including metal-coordinated anions, occur within α -Ni_{0.9}Al_{0.1}(OH)₂, can be synthetically controlled and correlate to electrochemical performance. Alkaline Ni–Zn sponge cells incorporating freestanding α -Ni_{0.9}Al_{0.1}(OH)₂@CNP cathodes deliver high discharge capacity, fast discharge times, excellent capacity retention, and greater than one electron per Ni at high mass loading.

2. Results and Discussion

2.1. The importance of architecture: Comparing powder composite and 3D architected cathodes

We adapt our microwave-assisted synthesis [18] to deposit alpha-phase, A^{13+} -substituted nickel hydroxide nanosheets (α -Ni_{0.9}Al_{0.1}(OH)₂ ns) onto conductive carbon nanofibers that comprise a current-collecting paper scaffold. In alkaline Ni–Zn sponge cells, we evaluate the electrochemical performance of the architected α -Ni_{0.9}Al_{0.1}(OH)₂ cathode against a conventional powder-composite cathode prepared using precipitated α -Ni_{0.9}Al_{0.1}(OH)₂ ns. Microwave-assisted synthesis offers a facile route to nanostructure and compositionally tune the nickel hydroxide active material. Under isotropic conditions and at mild pH, ultrathin polycrystalline, 2–12 nm thick nanosheets of α -Ni(OH)₂ coalesce into micron-sized agglomerates [18,49,50]. If we retain the reaction medium but add carbon nanofiber paper (CNP), the nanosheets nucleate and grow on the fibers (α -Ni_{0.9}Al_{0.1}(OH)₂@CNP). To improve the uniformity of the α -Al-Ni(OH)₂ deposited on the fibers, we use a pretreatment step (notated as PT: 1 h at 80 °C in the reaction medium) to equilibrate the Al/Ni precursors at the fibers before initiating the hydrolysis/condensation growth step. Without the pretreatment step, α -Ni_{0.9}Al_{0.1}(OH)₂ nanosheets deposit nonuniformly at the fibers and within the paper (Fig. S1, details provided in SI).

We can now evaluate the importance of electrode structure on the performance of microwave-synthesized α -Ni_{0.9}Al_{0.1}(OH)₂ nanosheets (*ns*) fabricated into a powder-composite structure versus deposited onto a freestanding architected electrode. The two electrode structures are illustrated graphically (Fig. 1a, b). The distinction between these two formulations is an ad hoc arrangement of electron-connected carbon agglomerates (Super P + carbon nanofibers) mixed with α -Ni_{0.9}Al_{0.1}(OH)₂ aggregated nanosheets (Fig. 1a) versus a binder-free architecture in which the nanosheets wrap the 3D-continuous electron conduit (Fig. 1b).

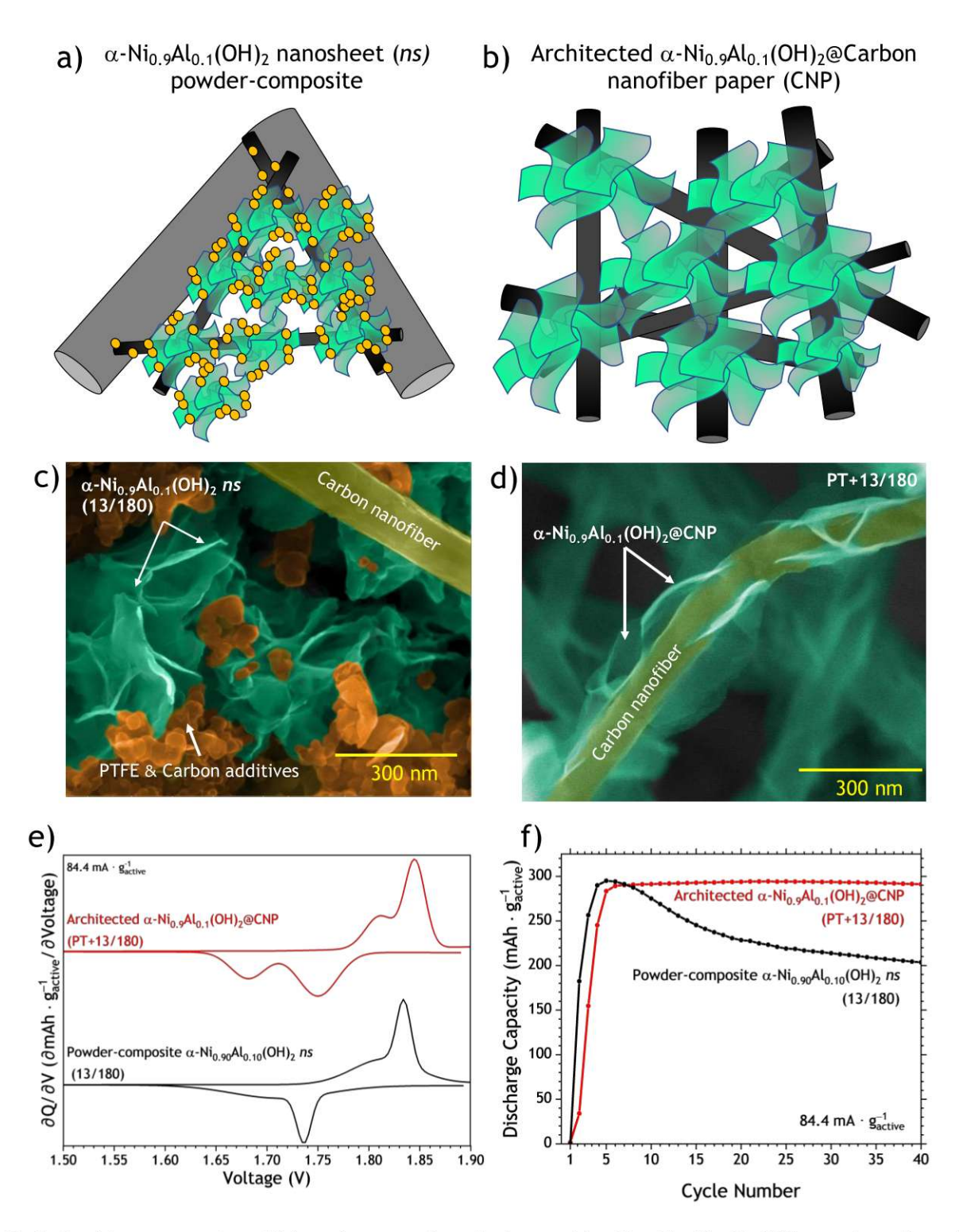


Fig. 1. Graphic representations of (a) powder-composite cathode comprising 65 wt% α -Ni_{0.9}Al_{0.1}(OH)₂ nanosheets (*ns*, colored green), 30 wt% particulate carbon (25 wt% Super P + 5 wt% carbon nanofibers), and 5 wt% PTFE binder in Ni foam (gray cylinders; carbon and PTFE, colored orange) and (b) Architected α -Ni_{0.9}Al_{0.1}(OH)₂@carbon nanofiber paper (α -Ni_{0.9}Al_{0.1}(OH)₂@CNP); (c) colorized scanning electron micrograph of a powder composite α -Ni_{0.9}Al_{0.1}(OH)₂ns (13/180) and (d) an architected α -Ni_{0.9}Al_{0.1}(OH)₂@CNP (PT+13/180); (e) 15th-cycle galvanostatic differential capacity analysis; and (f) discharge capacity versus cycle number of the cathodes at 84.4 mA g⁻¹_{active}, each with an active mass loading of 4 mg cm⁻². PT designates pretreating the CNF and CNP at 80°C in the precursor solution for 1 h (see Materials and Methods for details).

The powder-composite electrode is fabricated by mechanically mixing the conductive additives (Super P carbon and carbon nanofibers) with the electronically insulating α -Ni_{0.9}Al_{0.1}(OH)₂ (Ni(OH)₂: 10^{-17} S cm⁻¹; post-cycled Ni(OH)₂: 10^{-12} S cm⁻¹; NiOOH: 10^{-5} S cm⁻¹ [51]), and then adding an alkaline-resistant binder, forming an aqueous ink, and pasting into Ni foam (Fig. S2a). Scanning electron micrographs (SEM) and elemental mapping using energy-dispersive X-ray spectroscopy (EDS) show that formulating precipitated α -Ni_{0.9}Al_{0.1}(OH)₂ ns aggregates into a powder composite distributes the three components throughout the Ni foam without phase segregation occurring (Fig. 1c, Fig. S4). Within the powder composite, the α -Ni_{0.9}Al_{0.1}(OH)₂ (Fig. 1c, colored green; uncolored images shown in Fig. S3) has adventitious contact with the conductive additives (colored orange in Fig. 1a, Fig. S4b,c). When nucleated and grown onto the fibers of CNP (Fig. S2b), the α -Ni_{0.9}Al_{0.1}(OH)₂ wraps around the carbon nanofiber struts, obviating the need for a binder (Fig. 1d, colored green). This growth method pins the nanosheet directly to the electronically conductive CNP, rather than coalescing the nanosheets into the micron-sized aggregates obtained for solution-nucleated α -Ni_{0.9}Al_{0.1}(OH)₂ ns (Fig. 6a). To minimize material differences, α -Ni_{0.9}Al_{0.1}(OH)₂ growth is initiated using the same microwave time and temperature (13 min@180°C).

Matching the mass loading of α -Ni_{0.9}Al_{0.1}(OH)₂ in a powder composite and within an architected cathode at 4 mg cm⁻² gives us an opportunity to evaluate the effect of percolated versus direct electron wiring on charge-discharge performance in a Ni-Zn sponge cell (Fig. 1e, f). Differential capacity analysis of the powder-composite cathode shows a prominent Ni(OH)₂ oxidation peak at 1.84 V with a shoulder feature at 1.80 V and a NiOOH reduction peak (1.74 V) and shoulder feature (1.68 V); Fig. 1e. The presence of a primary peak with a shoulder is also observed in powder composites prepared using α -Ni(OH)₂ or metal-substituted α -Ni(OH)₂ [18]. Al³⁺ substitution stabilizes the α -phase in alkaline solutions but partial phase conversion to β-Ni(OH)₂ does occur, which could account for two electrochemically distinct Ni environments. The architected α-Ni_{0.9}Al_{0.1}(OH)₂@CNP shows two distinct, well-resolved oxidation peaks at 1.81 V and 1.85 V and two reduction peaks at 1.75 and 1.68 V that are more prominent than those observed for the powder composite (Fig. 1e). The two well-resolved peaks indicate two distinct reversible Ni-centered potential-energy environments exist within the architected material as it undergoes charge and discharge (eq. 2). Electron wiring and/or differences in the electronic environment of Ni sites, as we discuss below, may also influence the peak voltages and relative peak areas observed for α-Ni_{0.9}Al_{0.1}(OH)₂. The specific nature of the local environment of the two energetically distinct charge sites requires further study.

Both cathode structures initially show similar specific discharge capacity (Fig. 1f). By the 35th cycle, the architected α -Ni_{0.9}Al_{0.1}(OH)₂@CNP||Zn sponge cell retains its specific capacity (Fig. 1f) without an increase in charging voltage (Fig. S5a), while the cell with the powder-composite cathode suffers serious capacity fading, dropping by a third, even while imposing a higher charge voltage (Fig. S5a). The increased voltage required to charge the pasted powder-composite cathodes plus the severe capacity fade indicate impedance-driven polarization within the electrode structure. Although the powder composite and architected cathodes also have similar areal capacity at the 10th cycle, as cycling increases, the areal capacity of the architected cathode is maintained, clearly outperforming the powder-composite electrode structure (Fig. S5b). Within our 3D structure, directly wiring a thin coating of α -Ni_{0.9}Al_{0.1}(OH)₂ to the fibers in the CNP minimizes impedance, distributes the electro-reaction through the volume of the architected cathode, and lowers local current density thereby increasing heterogeneous electron-transfer kinetics, which aids reversibility of the Ni II/III/IV redox reactions—all of which contribute to improved cycling stability.

But does the cycling stability of the cell using an architected cathode primarily arise from improved electron-transfer kinetics between α -Ni_{0.9}Al_{0.1}(OH)₂ and the supporting carbon nanofiber? To evaluate this possibility, we formulate a powder composite replacing the non-networked α -Ni_{0.9}Al_{0.1}(OH)₂ ns with CNFs onto which a thin sheath of α -Ni_{0.9}Al_{0.1}(OH)₂ is microwave deposited (α -Ni_{0.9}Al_{0.1}(OH)₂@CNF, Fig. S6b). A Ni–Zn sponge cell assembled using this intermediate electrode formulation increases discharge capacity relative to powder-composited α -Ni_{0.9}Al_{0.1}(OH)₂ ns, but capacity again fades upon cycling (Fig. S6c), pointing to an electron-wiring problem within the volume of the cathode structure that an architected, 3D-wired cathode solves. We also evaluate the effect of α -Ni_{0.9}Al_{0.1}(OH)₂ ns mass loading on the discharge capacity of powder-composite cathodes, contrasting performance of cells using the low loadings typically found in the literature for 3D-wired carbons (1–3 mg cm⁻²) with device-relevant loadings (10 mg cm⁻²). Regardless of mass loading, all powder-composite formulations charge—discharged in Ni–Zn sponge cells exhibit similar near-linear discharge capacity fade with increasing cycle number (Fig. S6d).

2.2. Effect of time and temperature on the deposition and mass loading of α -Ni_{0.9}Al_{0.1}(OH)₂ in the architected carbon nanofiber paper

Using the two-step microwave protocol, we explore how varying time and temperature of the second step of the microwave reaction influences growth and mass loading. Scanning electron micrographs of α -Ni_{0.9}Al_{0.1}(OH)₂ deposited on the fibers in CNP using a pretreatment step (PT) and growth conditions of 13 min at 180°C (PT+13/180) reveal fiber-wired α -Ni_{0.9}Al_{0.1}(OH)₂ and un-wired, solution-nucleated, aggregated filtrates within the CNP (Fig. 2d–f). Optical micrographs show the agglomerated nanosheets at lower magnification (Fig. 2d). Lowering the temperature of the growth step from 180°C to 120°C (PT+13/120) significantly reduces the number of agglomerated nanosheets filtered out by the paper (Fig. 2d vs. Fig. 2g), while maintaining a uniform coating of α -Ni_{0.9}Al_{0.1}(OH)₂ on the fiber struts in the CNP (Fig. 2h–i). This lower-temperature growth step slows urea decomposition [50], minimizes the pH shift from acidic to basic, and prevents the internal pressurization that occurs in the reactor at 180°C (Fig. S7a vs Fig. S7b). The two-step reaction and lower reaction temperature may also affect the oxidation of the carbon surface and pH of the reaction solution as well as influence Ni nucleation at carbon nanofibers [52]. Maintaining a temperature of 120°C for the second step but increasing the reaction time from 13 to 120 min (PT+120/120) yields a thicker coating of α -Ni_{0.9}Al_{0.1}(OH)₂ nanosheets around the fibers in the CNP (Fig. 2k–l) and increases mass loading from 3.8 to 4.7 mg cm⁻² (Table S1).

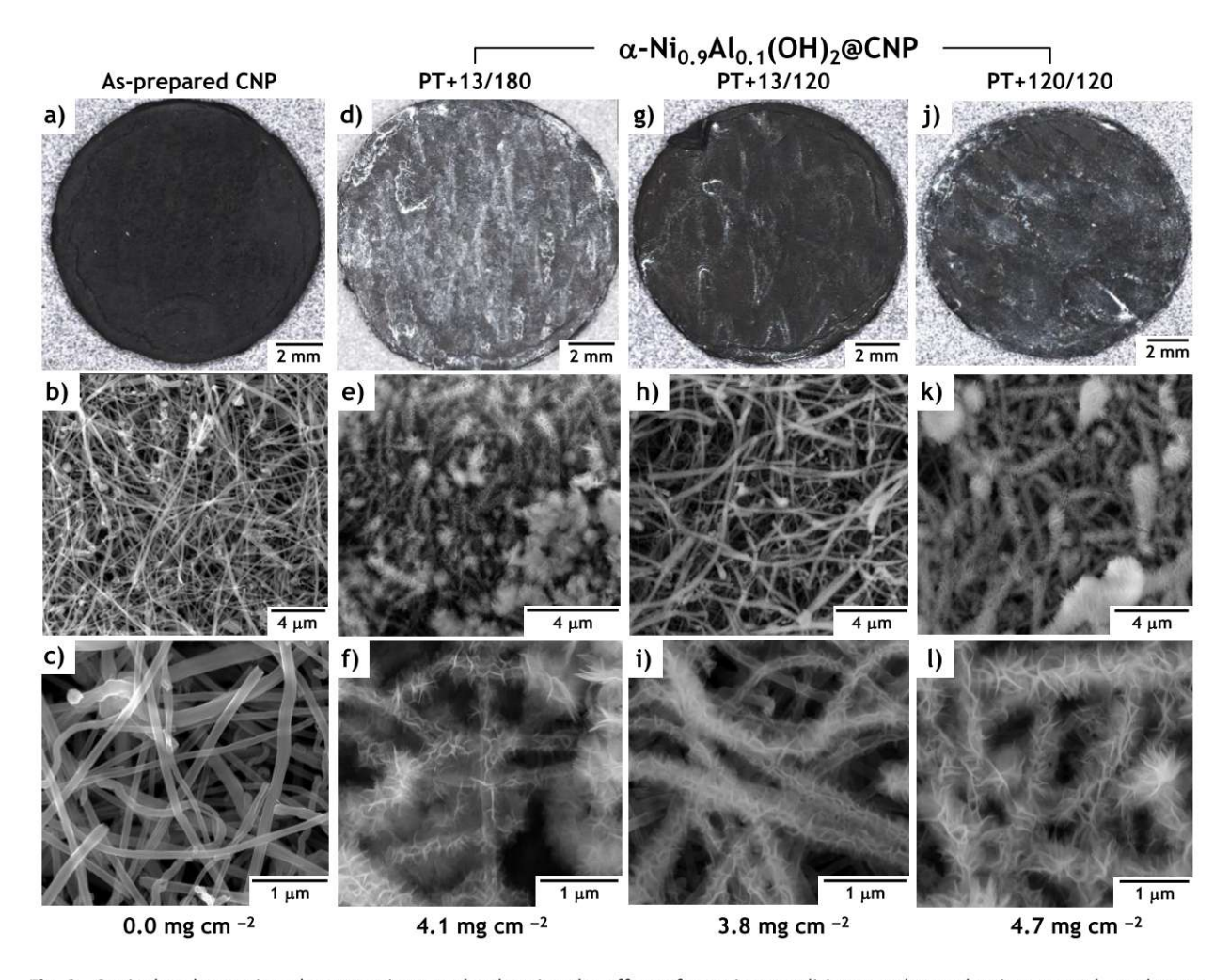


Fig. 2. Optical and scanning electron micrographs showing the effect of reaction conditions on the nucleation, growth, and mass loadings of α -Ni_{0.9}Al_{0.1}(OH)₂@CNP. (a–c) As-prepared CNP; (d–l) CNP pretreated at 80°C for 1 h (PT) before ramping to: (d–f) 180°C for 13 min (PT+13/180); (g–i) 120°C for 13 min (PT+13/120); and (j–l) 120°C for 120 min (PT+120/120).

2.3. Effect of growth temperature and time on the structure of α-Ni_{0.9}Al_{0.1}(OH)₂@CNP

Reaction time and temperature affect the chemical environment within the interlayer of microwave-synthesized α -Ni(OH)₂ nanosheets and thus the X-ray observable spacing [50]. We expect similar effects for architected α -Ni_{0.9}Al_{0.1}(OH)₂@CNP, in addition to changes in mass loading, plus possible electronic and surface chemistry effects. X-ray diffraction verifies that the nanosheets that agglomerate and precipitate out of isotropic medium as well as the nanosheets that deposit onto the fibers in CNP crystallize in the α -phase (Fig. 3a). As the microscopy establishes (Fig. 2), characterizing the architected cathodes convolves information from both fiber-wired α -Ni_{0.9}Al_{0.1}(OH)₂ and nanosheet aggregates captured within the CNP. The X-ray diffraction peak at ~10° 2 θ represents the (001) plane and corresponds to the c-axis of the unit cell, which describes the interlayer spacing, d₍₀₀₁₎ (Fig. 3b). Adding a pretreatment step before reacting for 13 min at 180°C broadens the (001) peak for α -Ni_{0.9}Al_{0.1}(OH)₂@CNP (PT+13/180) and slightly increases the interlayer spacing compared to precipitated α -Ni_{0.9}Al_{0.1}(OH)₂ ns (13/180); Fig. 3b, Table 1. The largest interlayer spacing (8.75 Å) is obtained for α -Ni_{0.9}Al_{0.1}(OH)₂ (PT+120/120). Similar trends for d₍₀₀₁₎ are obtained for the c-axis after fitting the diffractogram to obtain lattice parameters (Table 1). The different

interlayer spacings result from variations in the interlayer composition as supported by our Raman and XPS analyses, discussed below. Prior work also supports the expectation that interlayer composition affects interlayer spacing [18,50]. A (002) reflection is seen for all microwave-assisted variants except for α -Ni_{0.9}Al_{0.1}(OH)₂@CNP (PT+13/120), indicating that longer time and/or higher temperature are required to equilibrate the interlayer environment.

Fitting the X-ray diffractogram also reveals differences in crystallite domain sizes between α -Ni_{0.9}Al_{0.1}(OH)₂ ns and α -Ni_{0.9}Al_{0.1}(OH)₂@CNPs. The nanosheet morphology necessitates using two domain sizes, D₍₁₁₀₎, the domain size of nanosheet planes (in plane), and D₍₀₀₁₎, the domain size of stacked individual nanosheet planes (through plane), as illustrated graphically in Fig. 3c. The deposited nanosheets using the PT+13/180 protocol have a larger in-plane domain size D₍₁₁₀₎ and smaller through-plane D₍₀₀₁₎ compared to precipitated α -Ni_{0.9}Al_{0.1}(OH)₂ ns (13/180, Table 1). Reacting longer at a lower temperature (PT+120/120) results in a smaller in-plane domain size, D₍₁₁₀₎ for α -Ni_{0.9}Al_{0.1}(OH)₂@CNP.

Table 1. Physical characterization of precipitated α -Ni_{0.9}Al_{0.1}(OH)₂ nanosheets (*ns*: 13/180) and architected α -Ni_{0.9}Al_{0.1}(OH)₂@carbon nanofiber paper (α -Ni_{0.9}Al_{0.1}(OH)₂@CNP) by X-ray diffraction (d-spacing, lattice parameters, and crystallite size), Raman spectroscopy (peak area ratio of ν_1 (NO₃⁻, free) to ν_4 (NO₃⁻, bound)), and X-ray photoelectron spectroscopy (surface composition).

Sample Type	d-spacing Lattice parameters (Å) (Å)		Crystallite size (nm)		Raman peak area	Surface Composition (at.%)		
	d ₍₀₀₁₎	a=b	с	D ₍₀₀₁₎	D ₍₁₁₀₎	$v_1(NO_3^-$, free) to $v_4(NO_3^-$, bound)	Ni:Al	M(Ni+Al): Nitrogen
ns: 13/180	8.60	5.3	8.6	3.8	5.5	86:14	Ni _{0.89} Al _{0.11}	$M_{0.96}N_{0.04}$
CNP: PT+13/180	8.64	5.3	8.5	2.8	7.3	36:64	Ni _{0.84} Al _{0.16}	$M_{0.72}N_{0.28}$
CNP: PT+13/120	7.88	5.3	7.9	2.5	8.1	80:20	Ni _{0.88} Al _{0.12}	$M_{0.66}N_{0.34}$
CNP: PT+120/120	8.76	5.3	8.8	3.0	5.1	48:52	Ni _{0.85} Al _{0.15}	$M_{0.73}N_{0.27}$

X-ray photoelectron spectroscopy (XPS) survey spectra find an increase in relative nitrogen content of α -Ni_{0.9}Al_{0.1}(OH)₂@CNPs compared to the precipitated α -Ni_{0.9}Al_{0.1}(OH)₂ns (Table 1; Fig. S8). The atomic ratio of nitrogen to total metal content (Ni+Al) at the surface region significantly increases from 4% in α -Ni_{0.9}Al_{0.1}(OH)₂ ns (13/180) to 27–34% in the architected α -Ni_{0.9}Al_{0.1}(OH)₂@CNPs, indicating a higher concentration of nitrogenous species in the architected material. We observe Raman-active nitrate modes within two types of potential-energy environments, free and bound: ν_1 (NO₃⁻, free) at 1040–1046 cm⁻¹, [18,53], and ν_4 (NO₃⁻, bound) at 702–711 cm⁻¹ [18,53] (as shown in colored boxes in Fig. 3d and pictorially in Fig. 3c; see also Table S2). Peak broadening/splitting of the ν_4 (NO₃⁻, bound) mode (Fig. 3d and Table 1) can arise from different metal-bound nitrate environments or splitting due to changes in symmetry [54]. The nitrates originate from the precursor nickel and aluminum salts and can occupy sites within the interlayer and replace some metal-bound hydroxides [44]. Reaction time and temperature also affect the Raman-active lattice modes ν (α -Ni(OH)₂, E_g), shifting it to higher frequency in α -Ni_{0.9}Al_{0.1}(OH)₂@CNPs compared to α -Ni_{0.9}Al_{0.1}(OH)₂ns (13/180); small frequency-shift differences occur within the α -Ni_{0.9}Al_{0.1}(OH)₂@CNP series (Fig. 3e). The frequency shifts indicate changes to the local Ni–O bonding, with shifts to higher wavenumbers indicating a shorter Ni–O bond [55].

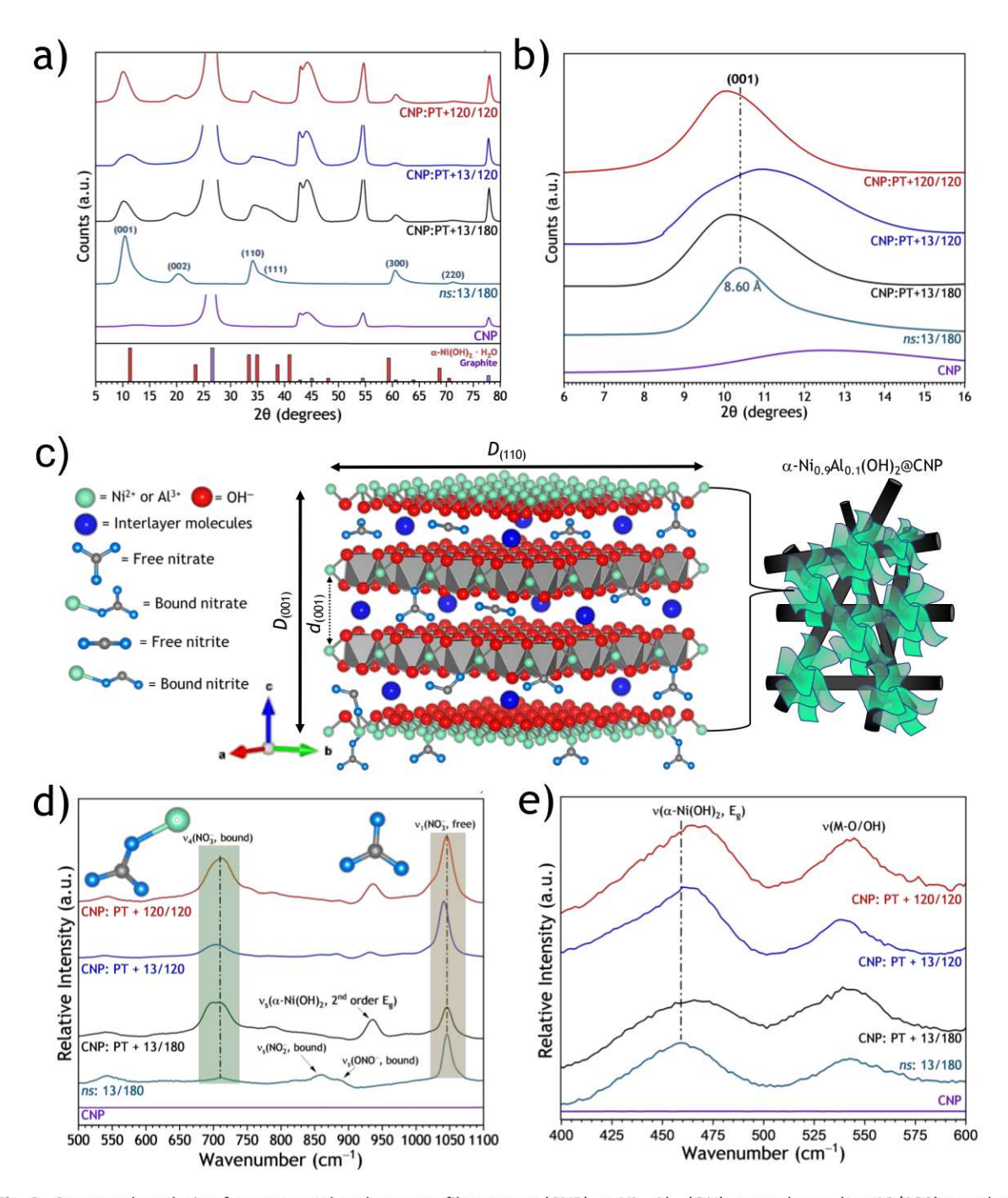


Fig. 3. Structural analysis of as-prepared carbon nanofiber paper (CNP), α -Ni_{0.9}Al_{0.1}(OH)₂ nanosheets (*ns*: 13/180) powder, and CNP pretreated at 80°C for 1 h (PT) before ramping to: 180°C for 13 min (PT+13/180); 120°C for 13 min (PT+13/120); and 120°C for 120 min (PT+120/120) using (a, b) X-ray diffraction and (d, e) Raman spectroscopy. (c) Graphic representation of the layered structure of α -Ni_{0.9}Al_{0.1}(OH)₂ nanosheets deposited on the fiber struts in the CNP; metals (nickel or aluminum, green), hydroxides (red) interlayer molecules (H₂O, ethylene glycol, and others, blue), interlayer nitrates, interlayer nitrites, bound nitrates, and bound nitrites represented in the structure were created using VESTA 3 [56]. Within this representation, the interlayer free and bound nitrates/nitrites and interlayer molecules do not occupy fixed crystallographic sites.

The ratio of the peak areas of $v_1(NO_3^-$, free): $v_4(NO_3^-$, bound) provides a measure of the nitrate speciation within the interlayer of α -Ni_{0.9}Al_{0.1}(OH)₂, expressed as either an agglomerated powder or nanoscopic coating (Fig. 3d, Table 1), recognizing that the different Raman cross sections of these modes influence absolute concentrations. Precipitated α -Ni_{0.9}Al_{0.1}(OH)₂ ns (13/180) contains predominately free nitrates (86%), whereas under all growth conditions, α -Ni_{0.9}Al_{0.1}(OH)₂@CNPs express a higher ratio of bound nitrates. Time and temperature conditions under to deposit the architected materials also affect the ratio of free-to-bound nitrates. Using lower growth temperature and increasing reaction time (PT+120/120) results in an almost equal ratio of free to bound nitrates (48% free nitrates). Nitrite (NO₂⁻) modes [57] are also present (Fig. 3e) with similar free-to-bound ratios seen for interlayer nitrates (Fig. S9, Table S2 and supporting text).

The differences in nitrogen speciation and surface concentration between α -Ni_{0.9}Al_{0.1}(OH)₂ms and the α -Ni_{0.9}Al_{0.1}(OH)₂@CNPs could arise from several factors including: (i) microwave-induced nitrogen doping of the graphite in CNF [58,59]; (ii) local microwave absorption/heating at the CNP [60] versus heating of the solution, preferentially raising the temperature at the carbon surface; and (iii) complex interactions in multi-metal hydrolysis/condensation reactions in metal nitrates influencing nitrogen speciation [61]. Additional analysis is needed to determine the primary driving factors affecting nitrogen environments in α -Ni_{0.9}Al_{0.1}(OH)₂@CNP.

2.4. Electrochemical performance of α -Ni_{0.9}Al_{0.1}(OH)₂@CNPs in Ni–Zn sponge cells

To test the electrochemical performance of the three architected α -Ni_{0.9}Al_{0.1}(OH)₂@CNPs prepared using different time/temperature growth conditions, we charge/discharge the cathodes at 100 mA g⁻¹_{active} in α -Ni_{0.9}Al_{0.1}(OH)₂@CNP||Zn sponge cells (0.5 mA cm⁻²). Unlike the powder composite (Fig. S5a), all three cells containing architected cathodes exhibit two-plateau discharge in the 15th cycle (Fig. 4a). However, the time/temperature synthetic conditions affect discharge capacity and charging efficacy. The cell containing the PT+120/120 cathode delivers the highest discharge capacity (305 mAh g⁻¹_{active}) and has the longest second discharge voltage plateau (~1.68 V). The cells containing PT+13/120 and PT+13/180 cathodes have lower discharge capacity within the second discharge voltage plateau.

The rate capability of architected α -Ni_{0.9}Al_{0.1}(OH)₂@CNP cathodes are evaluated using variable discharge rates between 100 and 3000 mA g⁻¹_{active}, but the same charge rate (Fig. 4b, c). The effective C-rate (Table S4), calculated from the discharge time, spans \sim C/3 (3 h) to 12C (5 min). All three architected variants exhibit remarkable rate capability, tapping \sim 90–97% of capacity at fast rates and recover the vast majority of the initial capacity on the return after the rate test (ART) to a slow discharge rate of 500 mA g⁻¹_{active} ART (Fig. 4b, c and Table S3). The cell with a PT+120/120 cathode shows the highest rate performance on a specific (Fig. 4b, c) and areal capacity basis (Fig. S10). The PT+120/120 cathode has a higher capacity (280 mAh g⁻¹ at 3000 mA g⁻¹_{active}) than either of the other two formulations at slow rates (100 mA g⁻¹_{active}). However, the cell equipped with a PT+13/120 cathode has the highest capacity retention (Fig. S11) and most stable rate performance (Fig 4b, c), which we attribute to thinner coatings and the lowest number of agglomerated, unwired α -Ni_{0.9}Al_{0.1}(OH)₂ nanosheets captured within the fiber paper (Fig. 4c, g). The high rate capacity is attributed to directly wiring the α -Ni_{0.9}Al_{0.1}(OH)₂ active material to the current-collecting architecture, enabling rapid and reversible delivery of electrons from 3 h to 5 min discharge times.

We then cycle the three rate-tested α -Ni_{0.9}Al_{0.1}(OH)₂@CNP cathodes for 60 cycles, discharging the Ni–Zn sponge cell at 500 mA g⁻¹_{active} and calculate the number of electrons stored per Ni atom using the

assayed amount of Ni in the architected cathode (Fig. 4d; calculation details provided in SI). The active material in commercial Ni cathodes, β -Ni(OH)₂ $\leftrightarrow \beta$ -NiOOH, maximally stores one electron per Ni resulting in a theoretical capacity of 289 mAh g^{-1}_{active} , based on 63.3 wt% Ni in Ni(OH)₂; commercially available β -Ni(OH)₂ typically is \sim 61 wt% Ni. The wt% of Ni within α -Ni_{0.9}Al_{0.1}(OH)₂ is much lower (44.1 wt% Ni, Table S1) due to replacing 10–13 atom % of lattice Ni with Al plus the added mass contributed by interlayer molecules in the structure [18,44]. All three α -Ni_{0.9}Al_{0.1}(OH)₂@CNPs store > 1 electron per Ni (e^- /Ni) over the 60 post–rate-test cycles (Fig. 4d). With a capacity retention of 96% (Fig. S11), the α -Ni_{0.9}Al_{0.1}(OH)₂@CNP (PT+13/120)||Zn sponge cell consistently stores > 1.3 e^- /Ni over the 60 cycles. Initially, the PT+120/120-equipped cell stores > 1.4 e^- /Ni but with a capacity retention of 94%, fades to 1.3 e^- /Ni by the 60th cycle. The α -Ni_{0.9}Al_{0.1}(OH)₂@CNP (PT+13/180)||Zn sponge cell has the lowest discharge capacity (Fig. 4d), but still stores >1.2 e^- /Ni.

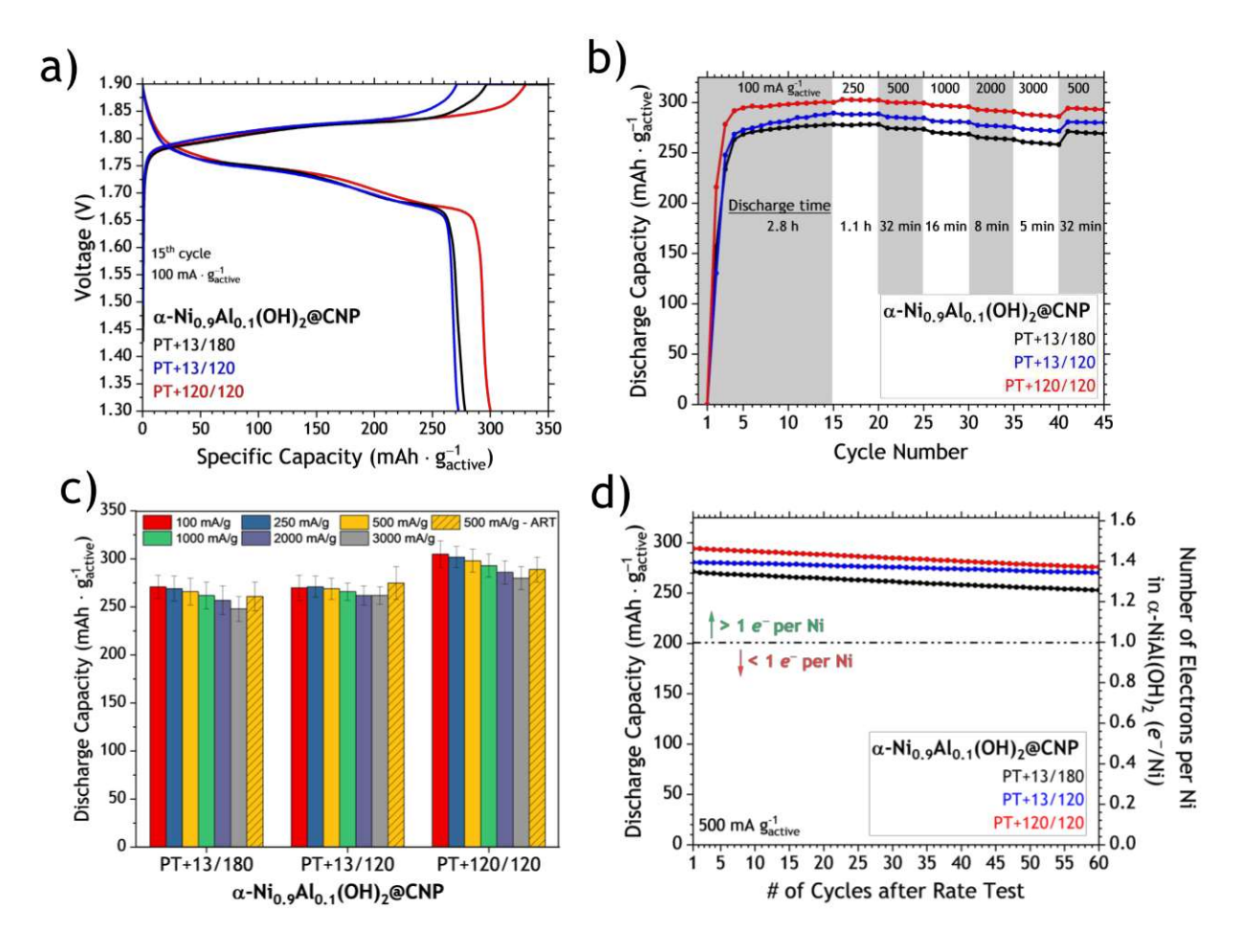


Fig. 4. Electrochemical performance of Ni–Zn cells with a Zn sponge anode versus an architected cathode prepared by pretreating CNP at 80°C for 1 h (PT) before ramping to: 180°C for 13 min (PT+13/180); 120°C for 13 min (PT+13/120); and 120°C for 120 min (PT+120/120): (a) 15th-cycle voltage profile of the Al-Ni(OH)₂@CNP||Zn sponge cells at 100 mA g^{-1}_{active} ; (b) discharge capacity and discharge times of the three α-Ni_{0.9}Al_{0.1}(OH)₂@CNP cathodes vs. Zn sponge at 100, 250, 500, 1000, 2000, 3000 mA g^{-1}_{active} before returning to 500 mA g^{-1}_{active} (ART: after rate test); (c) histogram summarizing the rate performance of the Ni–Zn sponge cells equipped with α-Ni_{0.9}Al_{0.1}(OH)₂@CNP cathodes; (d) Cycle stability of the three α-Ni_{0.9}Al_{0.1}(OH)₂@CNP after the rate rest as a function of discharge capacity (y₁ axis) and number of electrons stored per Ni in Al-Ni(OH)₂@CNP with 44.1 wt% Ni (y₂ axis).

The α -Ni_{0.9}Al_{0.1}(OH)₂@CNP (PT+120/120)||Zn sponge cell delivers the largest specific (Fig. 4a) and areal discharge capacity (Fig. S10) of the architected cathode formulations and was selected for long-term cycling analysis at charge and discharge rates of 100 mA g^{-1}_{active} and a cathode-limiting charge capacity of 350 mAh g^{-1}_{active} (Fig. S12). The cell has a discharge capacity of 303 mAh g^{-1}_{active} at the 15th cycle and 292 mAh g^{-1}_{active} at the 75th cycle, exhibiting excellent capacity retention (96%). Considering the wt% Ni and discharge capacity of 303 mAh g^{-1} for α -Ni_{0.9}Al_{0.1}(OH)₂@CNP, the microwave-derived architected active material stores 1.5 electrons per Ni maintaining > 1.4 e^- /Ni upon repeated charge—discharge cycles (Fig. S12).

The cell using a PT+120/120 architected cathode delivers the highest discharge capacity (Fig. 4a) but has the thickest coating on the nanofibers (Fig. 2) and the highest mass loading in the paper (Table S1), which is counterintuitive to conventional thinking that improved capacity with α -Ni(OH)₂/ γ -NiOOH is obtained using thinner coatings and lower mass loadings. The PT+120/120 CNP traps fewer unwired aggregates (Fig. 2j), has the largest interlayer d₍₀₀₁₎ spacing, larger D₍₀₀₁₎ through-plane nanocrystalline domains, a high nitrogen content, essentially equivalent free-to-bound nitrates, and a shorter Ni–O bond length (Fig. 4, Table 1). Our study supports the supposition that the ratio between free and bound nitrates is an important factor for the battery performance of architected α -Ni_{0.9}Al_{0.1}(OH)₂ cathodes in Ni–Zn sponge cells.

We posit that attaining and maintaining high discharge capacity when using architected cathodes results from the combination physicochemical factors such as effective 3D wiring of the active material, coating thickness, and structure, including interlayer distance, anion interactions, and electronic structure. An advantageous ratio of free and bound nitrates stabilizes the layered α -Ni(OH)₂, ameliorates electrostatic imbalances during charge/discharge, and contributes to more reversible electron transfer between Ni(III)/Ni(IV). Our thinking is in line with a prior study of Fe-substituted Ni(OH)₂ oxygen evolution electrocatalysts that report intercalated anions affect the electron density, lower the Gibbs energy for oxyhydroxide formation, and stabilize high-valent oxidation states of the metals [62].

The electrochemical performance of 3D-wired Ni-composite cathodes reported in the literature for Ni–Zn cells and that of Zn sponge cells using α -Al-Ni(OH)₂@CNP(PT+120/120) cathodes is summarized in Table S5 (supporting text in SI). Relative to other Ni-based cathodes used in rechargeable Ni–Zn cells, the α -Ni_{0.9}Al_{0.1}(OH)₂ (PT+120/120)||Zn sponge cell uniquely combines high discharge capacity and rate capability (303 and 287 mAh g⁻¹ at 0.1 and 1 A g⁻¹), excellent capacity retention (>94% and 96% at 0.5 and 0.1 A g⁻¹), and high mass loading (4.7 mg cm⁻²). A 3D α -Ni(OH)₂@Co/N-doped carbon paper has high capacity (302 mAh g⁻¹) in a Ni–Zn cell, but only at a much lower mass loading (\leq 1.0 mg cm⁻²) and with lower capacity retention (84%) [26]. The cell using the PT+120/120 architected cathode also delivers higher discharge capacity at higher mass loading compared to NiAlCo layered double hydroxide grown on carbon nanotubes (184 mAh g⁻¹ at 3.5 A g⁻¹ at 1 mg cm⁻²_{active} geometric loading in a Ni–Zn cell) [27].

3. Conclusions

Integrating electronic pathways to α -Ni_{0.9}Al_{0.1}(OH)₂ nanosheets throughout the volume of the carbon nanofoam paper improves capacity retention upon cycling in alkaline Ni–Zn sponge cells compared to powder-composite cathodes. Using a two-step reaction with a pretreatment step followed by a growth step and varying the time/temperature play a key role in controlling the uniformity of α -Ni_{0.9}Al_{0.1}(OH)₂ deposition on the nanofibers within the carbon scaffold. Increasing the time of the microwave

precipitation reaction at a lower temperature increases the coating thickness of α -Ni_{0.9}Al_{0.1}(OH)₂ on the fibers comprising the CNP and provides an architected cathode with 4.7 mg cm⁻² mass loading of active material. The nanosheet growth temperature and reaction time change the interlayer d₍₀₀₁₎ spacing and D₍₀₀₁₎ crystallite size, incorporate different concentrations of nitrogen-containing species, change the free-to-bound nitrate ratio, and alter the Ni–O bond length.

The architected α -Ni_{0.9}Al_{0.1}(OH)₂@CNP combines high discharge capacity, fast discharge times, excellent capacity retention, and high mass loading relative to other Ni-based cathodes for rechargeable Ni–Zn batteries. We attribute the excellent electrochemical performance of Ni–Zn sponge cells equipped with α -Ni_{0.9}Al_{0.1}(OH)₂@CNP cathodes to the combination of (*i*) thwarting agglomeration of α -Ni_{0.9}Al_{0.1}(OH)₂ nanosheets; (*ii*) electrically wiring α -Ni_{0.9}Al_{0.1}(OH)₂ onto the 3D-wired current-collecting carbon scaffold; and (*iii*) influencing the ratio of free-to-bound nitrate anions in the interlayer. A larger d₍₀₀₁₎ spacing and D₍₀₀₁₎ crystallite size, shorter Ni–O bond length, and an equal population of free and bound nitrates correlate to higher discharge capacity and more electrons stored per Ni. Designing architected electrodes that combine 3D electronic wiring with structures that utilize anions to control charge storage provides a pathway to high energy and power density rechargeable Ni–Zn batteries that rely on safe, inexpensive, earth-abundant battery chemistry. We also note that using coordinating and interlayer anions to facilitate charge storage provides a promising direction to improve electrochemical performance of a broad class of layered materials for multiple battery chemistries.

4. Materials and Methods

4.1. Materials Synthesis

Microwave synthesis of α-Ni_{0.9}Al_{0.1}(OH)₂ ns (13/180). The precipitated α-Ni_{0.9}Al_{0.1}(OH)₂ ns (13/180) was synthesized directly from an ethylene glycol/water solution containing nickel nitrate, aluminum nitrate, and urea, using a method adapted from our previous work [18,50], scaled for a high-throughput microwave reactor (Anton Parr Monowave 450). In the modified protocol, Ni(NO₃)₂ • 6H₂O (4.50 g, Ward Scientific), Al(NO₃)₂ • 9 H₂O (0.645, Acros Organics), and urea (4.10 g, Fisher Scientific) were added to a solution of ethylene glycol (105 mL, VWR) and ultrapure water (15 mL, ≥18 MΩ-cm, used for all subsequent reactions). The solution vessel was placed in an ice/water-filled bath sonicator and sonicated for 30 min, after which a homogenous solution (notated as Ni/Al stock solution) was obtained. 20 mL aliquots of the Ni/Al stock solution were transferred into a microwave-reaction vial (G30 Wide Neck Anton Paar microwave vials) with a polytetrafluoroethylene (PTFE) stir bar and sealed with a PTFE locking lid. The solution was exposed to instrument-controlled variable microwave power to maintain a reaction temperature of 180°C for 13 min (13/180) under magnetic stirring (600 rpm). The green precipitate was collected by centrifugation, washed five times with water and three times with ethanol (200 proof), centrifuged after each rinse, and then dried at 70°C for 21 h yielding α-Ni_{0.9}Al_{0.1}(OH)₂ (13/180) nanosheets.

Depositing α-Ni_{0.9}AI_{0.1}(OH)₂ onto carbon nanofibers (CNF). As-received carbon nanofibers (CNF, 100 nm × 20–200 μm; Sigma #719781-25G) were added to the microwave-reaction vials filled with 20 mL of the Ni/Al stock solution at a mass loading of 10 wt% CNF based on the average reaction yield of the Al-Ni(OH)₂ ns. The vial containing the suspension of CNFs in the Ni/Al solution was sonicated for 1 h. The solution was exposed to a two-step (pretreatment and growth step) variable microwave-induced heating protocol under magnetic stirring (600 rpm). First, the temperature was ramped to and held at 80°C for 60 min (PT), and then increased to 180°C and held for 13 min (13/180) before cooling to room

temperature. After the reaction was completed, the grey-green Al-Ni(OH)₂@CNF precipitate was collected by centrifugation, washed, and dried as described above.

Depositing Al³⁺-substituted a-Ni(OH)₂ nanosheets on carbon nanofiber paper (CNP). Carbon nanofiber paper (CNP) was fabricated by adapting a technique that vacuum filters a CNF/surfactant suspension to produce an architected carbon paper [63,64]. As-received carbon nanofibers (500 mg, Sigma) were added to a homogenous solution of a nonionic surfactant (Triton-X 100, 2 mL, Sigma # X100-100mL) and water (500 mL). The solution was placed in an ice/water bath and mixed using a wand sonicator (Sonics Vibracell VC505, 40% power) for 16 min at 10-s on/off intervals. The dispersion was vacuum filtered through a liquid nitrogen-cooled trap, and the resulting CNP was washed with 500 mL of water and dried under vacuum at 120°C for 21 h [65]. Conductivity measurements of the bare CNP were evaluated using a four-point probe (Liseis 3); conductivity was calculated from resistivity measured at 50 mA. The conductivity of the bare CNP is 0.75 S cm⁻¹, comparable to other nanofiber papers [63,64].

Electrodes (½" diameter) were punched out of the CNP and sewed into a PTFE mesh basket (McMaster-Carr, #1100T47) with PTFE fibers (McMaster-Carr, fibers unbraided from #1398T4). The basket was placed into a microwave-reaction vial with a PTFE stir bar, 20 mL of the Ni/Al stock solution, and sealed with a PTFE locking lid. The reaction was conducted using a two-step, one-pot pretreatment (PT) and growth protocol; the solution was heated to 80°C for 60 min (PT), then the temperature increased to either 120°C for 13 or 120 min or 180°C for 13 min. The baskets were collected, rinsed with water and ethanol, and then dried under vacuum at 120°C for 21 h.

Zinc-sponge anode. Fabrication of monolithic zinc-sponge anodes was adapted from previous work [8]. Briefly, 80 mg of high-viscosity sodium carboxymethyl cellulose (MilliporeSigma) was dissolved into 8 mL of water under constant stirring. Next, 3 g of IonSep CMC 52 preswollen carboxymethlycellulose resin (BIOpHORETICS) were dispersed into the mixture. The viscous slurry was manually stirred and agitated until homogenous, followed by adding 67.5 g of zinc powder (Umicore, 50 μm particles, containing 300 ppm Bi and 300 ppm In to suppress H₂ evolution). The resulting paste was pressed into rod-shaped molds and dried at 50°C overnight. To improve zinc particle bridging and remove the organic porogen, green-body zinc rods were heat treated at 400°C for 3 h in flowing nitrogen followed by a ramp at 2°C/min to 600°C in flowing air. Once the furnace reached 600°C, it was allowed to cool to ambient. Zinc-sponge disks were cut from the resulting rods and sanded to 1–2 mm in thickness.

4.2. Materials characterization

Microscopic evaluation and elemental analysis. The surface morphology of α-Ni_{0.9}Al_{0.1}(OH)₂ ns, α-Ni_{0.9}Al_{0.1}(OH)₂@CNF, and α-Ni_{0.9}Al_{0.1}(OH)₂@CNPs was characterized by scanning electron microscopy (SEM; Helios Nanolab 400). Optical micrographs of the α-Ni_{0.9}Al_{0.1}(OH)₂@CNPs were obtained using a Hirox digital microscope. Elemental analysis obtained using inductively coupled plasma—atomic emission spectroscopy (ICP—AES; Galbraith Laboratories, Knoxville, TN) was used to determine the composition in α-Ni_{0.9}Al_{0.10}(OH)₂ (13/180), α-Ni_{0.9}Al_{0.1}(OH)₂@CNF powders (PT+13/180), or α-Ni_{0.9}Al_{0.1}(OH)₂@CNP (PT+13/180). The mass loading of Ni in α-Ni_{0.9}Al_{0.1}(OH)₂@CNP was determined by acid digesting an entire ½" diameter electrode (microwave-assisted digestion, 2 h at 80 °C in 20 mL of 0.05 M HNO₃) and analyzing the solution using atomic-absorption (AA) spectroscopy (Perkin Elmer PinAAcle 900f, Ni lamp, λ=341.5 nm, slit width: 0.2 nm, gas & glow rate: compressed air at 10 L min⁻¹, acetylene at 2.5 L min⁻¹). Before acid digestion, the α-Ni_{0.9}Al_{0.1}(OH)₂@CNP was sonically broken apart (using a water-bath sonicator) inside a

microwave vial containing a 20-mL aliquot of 0.05 M HNO₃. After acid digestion, the dispersion was syringe filtered (Pall Laboratory, Acrodisc 28143-986); any remaining CNFs were further washed three times with 0.05 M HNO₃, reserving the supernatant after each wash. After digestion and washing, the Ni-containing solution was volumetrically diluted and the flame-atomic absorbance was measured vs a Ni(NO₃)₂ •·6 $H_2O/0.05$ M HNO₃ calibration curve.

The weight percentage of Ni from ICP and AA analysis, and the calculated wt% of active material and mass loading are presented in Table S1. The wt% of active material was calculated from the ICP and AA analyses; the digested nickel concentration was calculated from the AA measurement and the AA calibration curve. The wt% active material was derived from the ratio of Ni to total mass (either α -Ni_{0.9}Al_{0.1}(OH)₂ns or α -Ni_{0.9}Al_{0.1}(OH)₂@CNP). The geometric mass loading was determined from the total α -Ni_{0.9}Al_{0.1}(OH)₂@CNP mass, wt% active material in the α -Ni_{0.9}Al_{0.1}(OH)₂@CNP, and the area of the CNP.

Structure and chemical state analyses. X-ray diffraction patterns were collected (Bruker AXS D8 Advanced powder X-ray diffractometer, Cu K_{α} radiation source) over a 2θ scan range of 5–80° at a 0.01 step-increment. The diffractograms were analyzed using PDXL analysis software to remove $K\alpha_2$ and residual background signatures. The crystallographic lattice parameters of the α -Ni_{0.9}Al_{0.1}(OH)₂ ns (13/180) and the three α -Ni_{0.9}Al_{0.1}(OH)₂@CNP samples were calculated by fitting the diffraction patterns to the α -Ni(OH)₂ structure (ICDD 022-0444) originally proposed by Bode et al [66] using PDXL analysis software. Raman spectra were obtained using a 514 nm argon-ion laser line using a backscattering geometry and 600 nm groves/grating (Horiba LabRam HR evolution confocal spectrometer). The laser line was focused through a 50× long-range Olympus objective with a laser power controlled by a neutral density filter. To determine Raman peak area, the spectra were fit and integrated using Origin Pro (ver. Student 2023b). Survey and high-resolution X-ray photoelectron spectra (Thermo Fischer Scientific Nexsa XPS, monochromatic Al K α X-ray source) were collected using pass energies of 200 and 20 eV, respectively. The spectra were charge-shift corrected by fitting the most intense carbon peak to 284.8 eV as an internal calibration and analyzed using AVANTAGE v5.91 software (Thermo Fisher Scientific). Because surfaceadsorbed nitrates are sensitive to photoelectrons, [67] analysis of the nitrogen envelope was limited to survey spectra.

4.3. Electrochemical Characterization

Powder-Composite Cathodes. The α-Ni_{0.9}Al_{0.1}(OH)₂ ns (13/180) and α-Ni_{0.9}Al_{0.1}(OH)₂@CNF (PT+180) powders were fabricated into composite electrodes using a similar method previously described by our group for coin-cell cycling [18] with a ratio of 65 wt% active material / 30 wt% carbon / 5 wt% binder. To formulate the α-Ni_{0.9}Al_{0.1}(OH)₂ ns (13/180) composite, the 30 wt% of total conductive carbon comprised 25 wt% carbon black Super P (Alfa Aesar, #H30253) and 5 wt% as-received CNFs. The mass of CNF within the α-Ni_{0.9}Al_{0.1}(OH)₂@CNF (PT+180) composites offsets the mass of conductive carbon added to formulate the powder composite: the 30 wt% of total conductive carbon comprised 23.5 wt% Super P, and 6.5 wt% CNF from α-Ni_{0.9}Al_{0.1}(OH)₂@CNF (no additional CNF was added). The α-Ni_{0.9}Al_{0.1}(OH)₂ ns (13/180) or α-Ni_{0.9}Al_{0.1}(OH)₂@CNF (PT+180) materials were combined with the appropriate amounts of carbon and ground by hand in an agate mortar and pestle until well mixed. The black powder was transferred to a vial with 12–15 drops of water and sonicated (water-bath sonicator) for 10 min, the binder was added (PTFE Preparation, Sigma #665800-100mL) to the slurry, and sonicated for another 10 min. The slurry was vacuum infiltrated into acid-cleaned ½" Ni foam electrodes for 30 min before drying for 21 h under

ambient conditions. The powder-composite electrodes were pressed through a pasta roller (Imperia) and produced an electrode $\frac{1}{2}$ " in diameter.

 α -Ni_{0.9}Al_{0.1}(OH)₂||Zn sponge cell fabrication. The Ni–Zn cells were fabricated using reusable laser-cut, alkaline-resistant acrylic coin cells previously demonstrated by our group [2,8,9,18]. The cells contained a tin-foil current collector (0.25 mm thick, 99.8% Alfa Aesar), Zn-sponge anode, Celgard separator (3501), Freudenberg separator (700/28, electrolyte reservoir volume: 0.3–0.4 mL) [8], Ni cathode (either an architected α-Ni_{0.9}Al_{0.1}(OH)₂@CNP or powder-composited α-Ni_{0.9}Al_{0.1}(OH)₂ ns (13/180) or α-Ni_{0.9}Al_{0.1}(OH)₂@CNF (PT+180)), expanded Ni-mesh current collector (Dexmet), and a second Freudenberg separator within gas-tight ethylene propylene diene monomer (EDPM) gaskets and acrylic top and bottom plates. The α-Ni_{0.9}Al_{0.1}(OH)₂@CNP electrodes were first wrapped in expanded Ni-mesh (Dexmet) with a 1-cm tab and passed through the pasta roller before cell fabrication. The mass of active material, current collectors, binders, and additional conductive additives are presented in Fig. S13. A piece of ½" Ni foam was used as a spacer in the cells containing the α-Ni_{0.9}Al_{0.1}(OH)₂@CNP cathodes; placed between above the uppermost Freudenberg separator and the uppermost EDPM gasket. Before assembling into the cell, the Ni cathode and separators were vacuum infiltrated with 6 M KOH/1 M LiOH electrolyte and the Zn sponge was infiltrated for 30 min with a dispersion of 11 wt% Ca(OH)₂ in 6 M KOH/1 M LiOH.

The Ni–Zn cells were cycled using a constant current/constant voltage (CCCV) charging protocol between 1.30 and 1.90 V. During charge, a mass-normalized constant current (CC) was applied, if the cell reached 1.90 V before full charge (cathode capacity based on a theoretical capacity of 422 mA h g⁻¹active), the cell was held at a constant voltage (CV) until either fully charged or for up to 3 h, before discharging at a mass-normalized constant current. The wt% of α -Ni_{0.9}Al_{0.1}(OH)₂in α -Ni_{0.9}Al_{0.1}(OH)₂@CNP cathodes determined the mass-normalized currents. During constant-current galvanostatic cycling tests, the Ni electrodes were CCCV charged and discharged at 84.4 mA g⁻¹active (a 0.2C rate). Variable discharge-rate tests were conducted using the CCCV charge method [68]; during rate tests the charge-current was 100 mA g⁻¹active with discharge currents of 100 mA g⁻¹active for cycles 1–15, and 250, 500, 1000, 2000 and 3000 mA g⁻¹active for 5 cycles each before returning to a discharge rate of 500 mA g⁻¹active for cycles 40–100. The differential capacity of the Ni-cathodes was determined by taking the derivative of the mass-normalized capacity with respect to the cell voltage (Origin Pro) and fit using Origin's Fit Peak Pro, which uses a Levenberg–Marquardt algorithm. Long-term cycling of α -Ni_{0.9}Al_{0.1}(OH)₂@CNP synthesized using the two-step method of 1h@80°C→120m@120°C was made using CCCV charge and discharge at 100 mA g⁻¹active with a cathodic capacity of 350 mAh g⁻¹active.

Declaration of competing interest

C. P. R., S. W. K., D. R. R., and R. H. D. are inventors on a US Provisional Patent Application on architected Ni cathodes. R. H. D. and D. R. R. and hold a patent related to zinc electrodes: US Patent no. 11,710,818.

Credit authorship contribution statement

Samuel W. Kimmel: Conceptualization, Methodology, Investigation, Data curation, Formal analysis, Validation. Writing — original draft. Writing — review and editing. **Ryan H. DeBlock**: Conceptualization, Methodology, Formal Analysis, Writing — review and editing. **Jaret A. Manley:** Methodology, Investigation. **Cory M. Silguero:** Methodology, Investigation. **Debra R. Rolison**: Conceptualization, Funding acquisition, Formal analysis, Writing — review and editing. **Christopher P. Rhodes**: Conceptualization, Funding acquisition, Formal analysis, Writing — review and editing, Supervision.

Data availability

Data will be made available on request, pending approval from the sponsor and provided sufficient time is available.

Acknowledgments

This work was supported by the Office of Naval Research. S. W. K., D. R. R., and C. P. R. gratefully acknowledge additional support from the Office of Naval Research (Navy Undersea Research Program Grant No. N00014-21-1-2072) and the Naval Research Enterprise Internship Program. R. H. D. was an NRL—National Research Council Postdoctoral Associate (2020–2023). J. A. M. and C.M.S. acknowledge support from the National Science Foundation Partnerships for Research and Education in Materials Center for Intelligent Materials Assembly, Award No. 2122041 for materials synthesis and characterization.

Appendix A. Supplementary data

Supplementary data to this article can be found online at https://doi.org.

References

- Z. Yang, J. Zhang, M.C. Kintner-Meyer, X. Lu, D. Choi, J.P. Lemmon, J. Liu, Electrochemical Energy Storage for Green Grid, Chem. Rev. 111 (2011) 3577-3613. https://doi.org/10.1021/cr100290v
- 2. B.J. Hopkins, C.N. Chervin, M.B. Sassin, J.W. Long, D.R. Rolison, J.F. Parker, Low-Cost Green Synthesis of Zinc Sponge for Rechargeable, Sustainable Batteries, Sustain. Energy Fuels 4 (2020) 3363-3369. https://doi.org/10.1039/d0se00562b
- 3. R. Service, Zinc aims to beat lithium batteries at storing energy, Science 372 (2021) 890-891. https://doi.org/10.1126/science.372.6545.890
- 4. N. Niarchos, The Dark Side of Congo's Cobalt Rush, The New Yorker XCVII (2021) 40-49. https://www.newyorker.com/magazine/2021/05/31/the-dark-side-of-congos-cobalt-rush
- 5. Y. Chen, Y. Kang, Y. Zhao, L. Wang, J. Liu, Y. Li, Z. Liang, X. He, X. Li, N. Tavajohi, B. Li, A Review of Lithium-lon Battery Safety Concerns: The Issues, Strategies, and Testing Standards, J. Energy Chem. 59 (2021) 83-99. https://doi.org/10.1016/j.jechem.2020.10.017
- M. Huang, M. Li, C. Niu, Q. Li, L. Mai, Recent Advances in Rational Electrode Designs for High-Performance Alkaline Rechargeable Batteries, Adv. Funct. Mater. 29 (2019) 1-35. https://doi.org/10.1002/adfm.201807847
- 7. K.W. Beard, Linden's Handbook of Batteries, Fifth ed., McGraw-Hill Education, New York, 2019.
- 8. B.J. Hopkins, M.B. Sassin, C.N. Chervin, P.A. DeSario, J.F. Parker, J.W. Long, D.R. Rolison, Fabricating Architected Zinc Electrodes with Unprecedented Volumetric Capacity in Rechargeable Alkaline Cells, Energy Storage Mater. 27 (2020) 370-376. https://doi.org/10.1016/j.ensm.2020.02.005
- 9. B.J. Hopkins, M.B. Sassin, J.F. Parker, J.W. Long, D.R. Rolison, Zinc-Sponge Battery Electrodes that Suppress Dendrites, J. Vis. Exp. 163 (2020) E61770-E61780. https://doi.org/10.3791/61770
- J.S. Ko, A.B. Geltmacher, B.J. Hopkins, D.R. Rolison, J.W. Long, J.F. Parker, Robust 3D Zn Sponges Enable High-Power, Energy-Dense Alkaline Batteries, ACS Appl. Energy Mater. 2 (2018) 212-216. https://doi.org/10.1021/acsaem.8b01946
- 11. J.F. Parker, C.N. Chervin, E.S. Nelson, D.R. Rolison, J.W. Long, Wiring Zinc in Three Dimensions Re-Writes Battery Performance—Dendrite-Free Cycling, Energy Environ. Sci. 7 (2014) 1117-1124. https://doi.org/10.1039/c3ee43754j
- 12. J.F. Parker, C.N. Chervin, I.R. Pala, M. Machler, M.F. Burz, J.W. Long, D.R. Rolison, Rechargeable Nickel–3D Zinc Batteries: An Energy-Dense, Safer Alternative to Lithium-Ion, Science 356 (2017) 415-418. https://doi.org/10.1126/science.aak9991

- 13. J.F. Parker, E.S. Nelson, M.D. Wattendorf, C.N. Chervin, J.W. Long, D.R. Rolison, Retaining the 3D Framework of Zinc Sponge Anodes upon Deep Discharge in Zn–Air Cells, ACS Appl. Mater. Interfaces 6 (2014) 19471-19476. https://doi.org/10.1021/am505266c
- 14. D.R. Rolison, J.F. Parker, J.W. and Long. Zinc electrodes for batteries. US Patent: 9,802,254, *United States Patent and Trademark Office*, 10/31/2017.
- 15. D.R. Rolison, J.F. Parker, J.W. and Long. Zinc electrodes for batteries. US Patent: 10,008,711, United States Patent and Trademark Office, 06/26/2018.
- J. Li, E. Shangguan, D. Guo, M. Tian, Y. Wang, Q. Li, Z. Chang, X.-Z. Yuan, H. Wang, Synthesis, Characterization and Electrochemical Performance of High-Density Aluminum Substituted α-Nickel Hydroxide Cathode Material for Nickel-Based Rechargeable Batteries, J. Power Sources 270 (2014) 121-130. https://doi.org/10.1016/j.jpowsour.2014.07.098
- D.A. Corrigan, S.L. Knight, Electrochemical and Spectroscopic Evidence on the Participation of Quadrivalent Nickel in the Nickel Hydroxide Redox Reaction, J. Electrochem. Soc. 136 (1989) 613-619. https://doi.org/10.1149/1.2096697
- S.W. Kimmel, B.J. Hopkins, C.N. Chervin, N.L. Skeele, J.S. Ko, R.H. DeBlock, J.W. Long, J.F. Parker, B.M. Hudak, R.M. Stroud, D.R. Rolison, C.P. Rhodes, Capacity and Phase Stability of Metal-Substituted α-Ni(OH)₂ Nanosheets in Aqueous Ni–Zn Batteries Mater. Adv. 2 (2021) 3060-3074. https://doi.org/10.1039/D1MA00080B
- 19. R.W. Crocker, Structural Transformation of Nickel Hydroxide Films During Anodic Oxidation, Ph.D. dissertation, University of California, Lawrence Berkeley Labratory, Berkeley Ca, 1992. https://escholarship.org/uc/item/18k8b3xq
- L. Lai, R. Li, S. Su, L. Zhang, Y. Cui, N. Guo, W. Shi, X. Zhu, Controllable Synthesis of Reduced Graphene Oxide/Nickel Hydroxide Composites with Different Morphologies for High-Performance Supercapacitors, J. Alloys Compd. 820 (2020) 1-10. https://doi.org/10.1016/j.jallcom.2019.153120
- F. Lai, Y.E. Miao, L. Zuo, H. Lu, Y. Huang, T. Liu, Biomass-Derived Nitrogen-Doped Carbon Nanofiber Network: A Facile Template for Decoration of Ultrathin Nickel-Cobalt Layered Double Hydroxide Nanosheets as High-Performance Asymmetric Supercapacitor Electrode, Small 12 (2016) 3235-3244. https://doi.org/10.1002/smll.201600412
- L. Zhang, R. Chen, K.N. Hui, K.S. Hui, H. Lee, Hierarchical Ultrathin NiAl Layered Double Hydroxide Nanosheet Arrays on Carbon Nanotube Paper as Advanced Hybrid Electrode for High Performance Hybrid Capacitors, J. Chem. Eng. 325 (2017) 554-563. https://doi.org/10.1016/j.cej.2017.05.101
- 23. H. Yi, H. Wang, Y. Jing, T. Peng, Y. Wang, J. Guo, Q. He, Z. Guo, X. Wang, Advanced Asymmetric Supercapacitors Based on CNT@Ni(OH)₂ Core—Shell Composites and 3D Graphene Networks, J. Mater. Chem. A 3 (2015) 19545-19555. https://doi.org/10.1039/c5ta06174a
- 24. M. Huang, Z. Xu, C. Hou, S. Wang, Y. Zhuang, H.-l. Jia, M. Guan, Intermediate Phase α-β-Ni_{1-x}Co_x(OH)₂/Carbon Nanofiber Hybrid Material for High-Performance Nickel-Zinc Battery, Electrochim. Acta 298 (2019) 127-133. https://doi.org/10.1016/j.electacta.2018.12.094
- 25. Y. Jian, D. Wang, M. Huang, H.-L. Jia, J. Sun, X. Song, M. Guan, Facile Synthesis of Ni(OH)₂/Carbon Nanofiber Composites for Improving Ni-Zn Battery Cycling Life, ACS Sustain. 5 (2017) 6827-6834. https://doi.org/10.1021/acssuschemeng.7b01048
- 26. L. Zhu, B. Fei, Y. Xie, D. Cai, Q. Chen, H. Zhan, Engineering Hierarchical Co@N-Doped Carbon Nanotubes/alpha-Ni(OH)₂ Heterostructures on Carbon Cloth Enabling High-Performance Aqueous Nickel-Zinc Batteries, ACS Appl. Mater. Interfaces 13 (2021) 22304-22313. https://doi.org/10.1021/acsami.1c01711

- 27. M. Gong, Y. Li, H. Zhang, B. Zhang, W. Zhou, J. Feng, H. Wang, Y. Liang, Z. Fan, J. Liu, H. Dai, Ultrafast High-Capacity NiZn Battery with NiAlCo-Layered Double Hydroxide, Energy Environ. Sci. 7 (2014) 2025–2032. https://doi.org/10.1039/c4ee00317a
- 28. S.P. Lonkar, J.M. Raquez, P. Dubois, One-Pot Microwave-Assisted Synthesis of Graphene/Layered Double Hydroxide (LDH) Nanohybrids, Nano-micro Lett. 7 (2015) 332-340. https://doi.org/10.1007/s40820-015-0047-3
- W. He, H. Qiu, J. Meng, B. Liu, J. Cui, Y. Zhang, Microwave-Assisted Synthesis of Nano Petal-Like α-Ni(OH)2/RGO and its Electrochemical Performance, J. Alloys Compd. 788 (2019) 183-190. https://doi.org/10.1016/j.jallcom.2019.02.111
- 30. Y. Kim, E.-s. Cho, S.-J. Park, S. Kim, One-Pot Microwave-Assisted Synthesis of Reduced Graphene Oxide/Nickel Cobalt Double Hydroxide Composites and Their Electrochemical Behavior, J. Ind. Eng. Chem. 33 (2016) 108-114. https://doi.org/10.1016/j.jiec.2015.09.023
- 31. S. Bag, C.R. Raj, Layered Inorganic–Organic Hybrid Material Based on Reduced Graphene Oxide and α-Ni(OH)₂ for High Performance Supercapacitor Electrodes, J. Mater. Chem. A 2 (2014) 17848-17856. https://doi.org/10.1039/c4ta02937b
- 32. J. Xu, S. Gai, F. He, N. Niu, P. Gao, Y. Chen, P. Yang, Reduced Graphene Oxide/Ni_(1-x)Co_(x)Al-Layered Double Hydroxide Composites: Preparation and High Supercapacitor Performance, Dalton Trans. 43 (2014) 11667-11675. https://doi.org/10.1039/c4dt00686k
- 33. A.L. Brisse, P. Stevens, G. Toussaint, O. Crosnier, T. Brousse, Ni(OH)₂ and NiO Based Composites: Battery Type Electrode Materials for Hybrid Supercapacitor Devices, Materials 11 (2018) 1-15. https://doi.org/10.3390/ma11071178
- 34. H. Sun, J. Zhu, D. Baumann, L. Peng, Y. Xu, I. Shakir, Y. Huang, X. Duan, Hierarchical 3D Electrodes for Electrochemical Energy Storage, Nat. Rev. Mater. 4 (2018) 45-60. https://doi.org/10.1038/s41578-018-0069-9
- D.R. Rolison, J.W. Long, J.C. Lytle, A.E. Fischer, C.P. Rhodes, T.M. McEvoy, M.E. Bourg, A.M. Lubers, Multifunctional 3D Nanoarchitectures for Energy Storage and Conversion, Chem. Soc. Rev. 38 (2009) 226-252. https://doi.org/10.1039/b801151f
- M.B. Sassin, C.N. Chervin, D.R. Rolison, J.W. Long, Redox Deposition of Nanoscale Metal Oxides on Carbon for Next-Generation Electrochemical Capacitors, Acc. Chem. Res. 46 (2013) 1062-1071. https://doi.org/10.1021/ar2002717
- 37. J.W. Long, B. Dunn, D.R. Rolison, H.S. White, Three-Dimensional Battery Architectures, Chem. Rev. 104 (2004) 4463-4492. https://doi.org/10.1021/cr020740l
- 38. C. Lamiel, V.H. Nguyen, D.R. Kumar, J.-J. Shim, Microwave-Assisted Binder-Free Synthesis of 3D Ni-Co-Mn Oxide Nanoflakes@Ni Foam Electrode for Supercapacitor Applications, Chem. Eng. J. 316 (2017) 1091-1102. https://doi.org/10.1016/j.cej.2017.02.004
- 39. C. Lamiel, V.H. Nguyen, I. Hussain, J.-J. Shim, Enhancement of electrochemical performance of nickel cobalt layered double hydroxide@nickel foam with potassium ferricyanide auxiliary electrolyte, Energy 140 (2017) 901-911. https://doi.org/10.1016/j.energy.2017.09.035
- 40. Y. Zhang, Q. Shao, S. Long, X. Huang, Cobalt-Molybdenum Nanosheet Arrays as Highly Efficient and Stable Earth-Abundant Electrocatalysts for Overall Water Splitting, Nano Energy 45 (2018) 448-455. https://doi.org/10.1016/j.nanoen.2018.01.022
- 41. S. Sahoo, T.T. Nguyen, J.-J. Shim, Mesoporous Fe–Ni–Co ternary oxide nanoflake arrays on Ni foam for high-performance supercapacitor applications, J. Ind. Eng. Chem. 63 (2018) 181-190. https://doi.org/10.1016/j.jiec.2018.02.014
- T. Liang, H. Xuan, Y. Xu, J. Gao, X. Han, J. Yang, P. Han, D. Wang, Y. Du, Rational Assembly of CoAl-Layered Double Hydroxide on Reduced Graphene Oxide with Enhanced Electrochemical Performance for Energy Storage, ChemElectroChem 5 (2018) 2424-2434. https://doi.org/10.1002/celc.201800510

- 43. B. Liu, X. Liu, X. Fan, J. Ding, W. Hu, C. Zhong, 120 Years of Nickel-Based Cathodes For Alkaline Batteries, J. Alloys Compd. 834 (2020) 1-11. https://doi.org/10.1016/j.jallcom.2020.155185
- 44. D.S. Hall, D.J. Lockwood, C. Bock, B.R. MacDougall, Nickel Hydroxides and Related Materials: A Review of Their Structures, Synthesis and Properties, Proc. R. Soc. A 471 (2015) 1-65. https://doi.org/10.1098/rspa.2014.0792
- 45. Y.W. Li, J.H. Yao, C.J. Liu, W.M. Zhao, W.X. Deng, S.K. Zhong, Effect of Interlayer Anions on the Electrochemical Performance of Al-Substituted α-Type Nickel Hydroxide Electrodes, Int. J. Hydrog. Energy 35 (2010) 2539-2545. http://doi.org/10.1016/j.ijhydene.2010.01.015
- 46. E. Shangguan, J. Li, D. Guo, L. Guo, M. Nie, Z. Chang, X.-Z. Yuan, H. Wang, A Comparative Study of Structural and Electrochemical Properties of High-Density Aluminum Substituted α-Nickel Hydroxide Containing Different Interlayer Anions, J. Power Sources 282 (2015) 158-168. http://doi.org/10.1016/j.jpowsour.2015.02.059
- 47. J.W. Lee, J.M. Ko, J.-D. Kim, Hierarchical Microspheres Based on α-Ni(OH)₂ Nanosheets Intercalated with Different Anions: Synthesis, Anion Exchange, and Effect of Intercalated Anions on Electrochemical Capacitance, J. Phys. Chem. C 115 (2011) 19445-19454. http://doi.org/10.1021/jp206379h
- 48. S. Fu, L. Li, Y. Zhang, S. Chen, S. Fang, Y. Jing, G. Li, Anion De/Intercalation in Nickel Hydroxychloride Microspheres: A Mechanistic Study of Structural Impact on Energy Storage Performance of Multianion-Containing Layered Materials, ACS Appl. Energy Mater. 1 (2018) 1522-1533. http://doi.org/10.1021/acsaem.7b00324
- 49. S.W. Kimmel, B.D. Koehne, B. Gibson, W.J. Geerts, N. Theodoropoulou, C.P. Rhodes, Structure and Magnetism of Iron-Substituted Nickel Hydroxide Nanosheets, Magnetochemistry 9 (2023) 25-47. https://doi.org/10.3390/magnetochemistry9010025
- 50. S.W. Kimmel, V.L. Kuykendall, C.F. Mough, A. Landry, C.P. and Rhodes, Effect of Microwave Synthesis Conditions on the Structure of Nickel Hydroxide Nanosheets, J. Vis. Exp. 198 (2023) 1-21. https://doi.org/10.3791/65412
- 51. A. Motori, F. Sandrolini, Electrical Properties of Nickel Hydroxide for Alkaline Cell Systems, J. Power Sources 48 (1994) 361-370. https://doi.org/10.1016/0378-7753(94)80032-4
- 52. M.K. Van der Lee, A. Jos van Dillen, J.H. Bitter, K.P. and de Jong, Deposition Precipitation for the Preparation of Carbon Nanofiber Supported Nickel Catalysts, J. Am. Chem. Soc 127 (2005) 13573-13582. https://doi.org/10.1021/ja053038q
- 53. D.S. Hall, D.J. Lockwood, S. Poirier, C. Bock, B.R. MacDougall, Raman and Infrared Spectroscopy of Alpha and Beta Phases of Thin Nickel Hydroxide Films Electrochemically Formed on Nickel, J. Phys. Chem. A 116 (2012) 6771-6784. http://doi.org/10.1021/jp303546r
- 54. J.L. Bishop, S.J. King, M.D. Lane, A.J. Brown, B. Lafuente, T. Hiroi, R. Roberts, G.A. Swayze, J.F. Lin, M. Sánchez Román, Spectral Properties of Anhydrous Carbonates and Nitrates, Earth Space Sci. 8 (2021). http://doi.org/10.1029/2021ea001844
- D. Chen, X. Xiong, B. Zhao, M.A. Mahmoud, M.A. El-Sayed, M. Liu, Probing Structural Evolution and Charge Storage Mechanism of NiO₂H_x Electrode Materials using In Operando Resonance Raman Spectroscopy, Adv. Sci. 3 (2016) 1500433-1500436. http://doi.org/10.1002/advs.201500433
- K. Momma, F. Izumi, VESTA 3 for Three-Dimensional Visualization of Crystal, Volumetric and Morphology Data, J. Appl. Crystallogr. 44 (2011) 1272-1276. https://doi.org/10.1107/S0021889811038970
- 57. M.H. Brooker, Infra-red and Raman Spectral Study of the Aqueous Nickel(II)-Nitrite System, J. Chem. Soc., Faraday Trans. 1 71 (1974) 647-656. http://doi.org/10.1039/F19757100647
- 58. T. Kondo, S. Casolo, T. Suzuki, T. Shikano, M. Sakurai, Y. Harada, M. Saito, M. Oshima, M.I. Trioni, G.F. Tantardini, J. Nakamura, Atomic-scale Characterization of Nitrogen-Doped Graphite: Effects

- of Dopant Nitrogen on the Local Electronic Structure of the Surrounding Carbon Atoms, Phys. Rev. B 86 (2012). http://doi.org/10.1103/PhysRevB.86.035436
- 59. X. Wang, X. Li, L. Zhang, Y. Yoon, P.K. Weber, H. Wang, J. Guo, H. Dai, N-Doping of Graphene Through Electrothermal Reactions with Ammonia, Science 324 (2009) 768-771. https://www.doi.org/10.1126/science.1170335
- 60. E. Pérez-Botella, D. Peumans, G. Vandersteen, G.V. Baron, J.M. Catalá-Civera, J.D. Gutiérrez-Cano, G. Van Assche, A. Costa Cornellà, J.F.M. Denayer, Challenges in the microwave heating of structured carbon adsorbents, J. Chem. Eng. 476 (2023). http://doi.org/10.1016/j.cej.2023.146632
- 61. E.A. Cochran, K.N. Woods, D.W. Johnson, C.J. Page, S.W. Boettcher, Unique Chemistries of Metal-Nitrate Precursors to Form Metal-Oxide Thin Films from Solution: Materials for Electronic and Energy Applications, J. Mater. Chem. A 7 (2019) 24124-24149. http://doi.org/10.1039/c9ta07727h
- D. Zhou, Z. Cai, Y. Bi, W. Tian, M. Luo, Q. Zhang, Q. Zhang, Q. Xie, J. Wang, Y. Li, Y. Kuang, X. Duan, M. Bajdich, S. Siahrostami, X. Sun, Effects of Redox-Active Interlayer Anions on the Oxygen Evolution Reactivity of NiFe-Layered Double Hydroxide Nanosheets, Nano Res. 11 (2018) 1358-1368. http://doi.org/10.1007/s12274-017-1750-9
- 63. H. Lu, Y. Liu, J. Gou, J. Leng, S. Du, Electrical Properties and Shape-Memory Behavior of Self-Assembled Carbon Nanofiber Nanopaper Incorporated with Shape-Memory Polymer, Smart Mater. Struct. 19 (2010) 1-7. https://doi.org/10.1088/0964-1726/19/7/075021
- 64. H. Lu, Y. Liu, J. Gou, J. Leng, S. Du, Electroactive Shape-Memory Polymer Nanocomposites Incorporating Carbon Nanofiber Paper, Int. J. Smart Nano. Mater. 1 (2010) 2-12. https://doi.org/10.1080/19475411003612749
- 65. S.W. Kimmel, R.H. DeBlock, J.A. Manley, B.M. Gibson, C.M. Silguero, D.R. Rolison, C.P. Rhodes, Designing High Discharge Capacity and High-Rate Nickel Hydroxide Cathodes for Rechargeable Alkaline Nickel–Zinc Batteries, Proceedings of the 49th Power Sources Conference 37 (2023) 25-23.
- 66. V.H. Bode, K. Dehmelt, J. Witte, Uber die Oxydationsprodukte von Nickel(II)-hydroxiden, Z. Anorg. Allg. Chem. 366 (1969) 1-21. https://doi.org/10.1002/zaac.19693660102
- 67. C.E. Nanayakkara, P.M. Jayaweera, G. Rubasinghege, J. Baltrusaitis, V.H. Grassian, Surface photochemistry of adsorbed nitrate: the role of adsorbed water in the formation of reduced nitrogen species on alpha-Fe₂O₃ particle surfaces, J. Phys. Chem. A 118 (2014) 158-166. http://doi.org/10.1021/jp409017m
- 68. M. Casas-Cabanas, J.C. Hernandez, V. Gil, M.L. Soria, M.R. Palacín, Rationalization of the Industrial Nickel Hydroxide Synthetic Process in View of Optimizing its Electrochemical Performances, Ind. Eng. Chem. Res. 43 (2004) 4957-4963. https://doi.org/10.1021/ie034282y